



#### **OPEN ACCESS**

EDITED BY Shihua Shi, Friedrich Miescher Institute for Biomedical Research (FMI), Switzerland

David Magne, Université de Lyon, France GIL Goobes. Bar-Ilan University, Israel

\*CORRESPONDENCE Jingting Yao oxdim jy1015@mgh.harvard.edu

RECEIVED 20 August 2025 REVISED 16 October 2025 ACCEPTED 05 November 2025 PUBLISHED 26 November 2025

Yao J, Farrar CT, Aikawa E, Sosnovik DE, Moon BF, Kulkarni A and Ackerman JL (2025) Ex vivo phosphorus-31 solid state magnetic resonance spectroscopy identifies compositional differences between bone mineral and calcified vascular tissues Front. Cardiovasc. Med. 12:1689116. doi: 10.3389/fcvm.2025.1689116

© 2025 Yao, Farrar, Aikawa, Sosnovik, Moon, Kulkarni and Ackerman. This is an openaccess article distributed under the terms of the Creative Commons Attribution License (CC BY). The use, distribution or reproduction in other forums is permitted, provided the original author(s) and the copyright owner(s) are credited and that the original publication in this journal is cited, in accordance with accepted academic practice. No use, distribution or reproduction is permitted which does not comply with these terms.

# Ex vivo phosphorus-31 solid state magnetic resonance spectroscopy identifies compositional differences between bone mineral and calcified vascular tissues

Jingting Yao<sup>1,2\*</sup>, Christian T. Farrar<sup>1,2</sup>, Elena Aikawa<sup>2,3,4</sup>, David E. Sosnovik<sup>1,2,5</sup>, Brianna F. Moon<sup>1,2,5</sup>, Aditi Kulkarni<sup>1</sup> and Jerome L. Ackerman<sup>1,2</sup>

<sup>1</sup>Athinoula A. Martinos Center for Biomedical Imaging, Massachusetts General Hospital, Charlestown, MA, United States, <sup>2</sup>Radiology Department, Harvard Medical School, Boston, MA, United States, <sup>3</sup>Center for Interdisciplinary Cardiovascular Sciences, Division of Cardiovascular Medicine, Brigham and Women's Hospital, Harvard Medical School, Boston, MA, United States, <sup>4</sup>Center for Excellence in Vascular Biology, Division of Cardiovascular Medicine, Brigham and Women's Hospital, Harvard Medical School, Boston, MA, United States, <sup>5</sup>Cardiovascular Research Center, Massachusetts General Hospital, Charlestown, MA, United States

Aim: Physiological bone mineralization and ectopic vascular calcification share similarities in the composition of calcium phosphate minerals. Evidence suggests a connection between the underlying biological mechanisms driving the deposition of bone mineral and cardiovascular calcification. Therefore, understanding the chemistry and composition of bone mineral and vascular calcification may be important for the development of effective treatments and diagnostic tools for cardiovascular diseases, as pharmacological interventions for the treatment of one process might affect the other. The goal of this study was to identify and compare compositional features of calcium phosphates in bone and calcified vascular tissues using phosphorus-31 (31P) solid state cross-polarization magic angle spinning (CPMAS) magnetic resonance (MR) spectroscopy, a specialized technique that provides compositional information unattainable through conventional chemical analysis.

Methods: Solid state MR spectra were acquired from biological specimens of human trabecular bone (n = 1), human vascular plaque (n = 1), human calcified aortic valves (n = 5), as well as calcified aortic tissues of apolipoprotein E-deficient mice (n = 1) fed a high cholesterol diet. Synthetic hydroxyapatite [Ca<sub>10</sub>(OH)<sub>2</sub>(PO<sub>4</sub>)<sub>6</sub>] and synthetic brushite (CaHPO<sub>4</sub>·2H<sub>2</sub>O) were used to model the solid state  $^{31}P$  MR spectra of the phosphate ion  $PO_4^{-3}$  and hydrogen phosphate ion HPO<sub>4</sub><sup>-2</sup>, respectively. Qualitative spectral features and quantitative metrics derived using Herzfeld-Berger analysis were assessed to characterize mineral composition and maturity.

Results: Solid state <sup>31</sup>P MR spectra of all human specimens studied suggested a well-ordered crystal structure dominated by unprotonated phosphate (PO<sub>4</sub><sup>-3</sup>), consistent with mature bone-like mineral. These specimens exhibited long CP time constants (700-900 µs) and modest chemical shift anisotropy. In contrast, the calcified mouse aorta spectrum showed pronounced sidebands, a short CP time constant (~270  $\mu$ s), and a more prominent HPO<sub>4</sub><sup>-2</sup> component-features indicative of immature, newly deposited mineral.

**Conclusion:** <sup>31</sup>P solid state MR spectroscopy reveals differences in the phosphate and hydrogen phosphate ion content among the calcified tissues studied. This technique could potentially be an important complement to basic studies of pathological calcification in atherosclerosis and related calcific disorders.

KEYWORDS

calcium phosphate, hydroxyapatite, magnetic resonance spectroscopy, plaque, vascular calcification

### 1 Introduction

Physiological bone mineralization and pathological vascular calcification exhibit some similarities in their underlying mechanisms and calcium phosphate mineral composition (1, 2). Although the two processes are physiologically distinct, they share some cellular pathways and molecular mediators, including common proteins and regulatory factors (3-9). Inflammation and macrophage activities are key drivers of vascular calcification, and osteoclasts—the bone-resorbing cells originate from the same hematopoietic lineage as macrophages (10, 11). Epidemiological studies have reported associations between osteoporosis and increased cardiovascular risk (12). Clinical observations further support this biological linkage: pharmacological agents used to treat cardiovascular diseases (CVDs) can influence bone metabolism, and conversely, treatments for osteoporosis may affect vascular calcification (13-15). Specifically, bisphosphonates (BPs), the most common anti-osteoporotic agents, inhibit bone resorption by binding to hydroxyapatite and suppressing osteoclast activity (16). BPs are non-hydrolyzable analogs of inorganic pyrophosphate, an endogenous inhibitor of vascular calcification (17, 18). BPs have been linked to altered lipid profiles and reduced aortic calcification (19). Moreover, statins have shown associations with increased bone mineral density (15). Estrogen deficiency, which accelerates bone loss, is also a known risk factor for atherosclerosis and vascular calcification (20, 21).

Vascular calcification is a key feature of atherosclerosis and a well-established predictor of cardiovascular events. While coronary artery calcium scores reflect total calcium burden, studies suggest that the chemical composition and structural organization of calcium deposits may more directly influence plaque stability and clinical outcomes (22–28). Beyond serving as a risk marker, mineral composition may reflect distinct stages of plaque development with differing biological implications, potentially clarifying mechanisms of disease and inform the design of targeted therapies aimed at specific phases of calcification.

In vertebrates, the final mineral product of biomineralization is a poorly crystalline, nonstoichiometric form of hydroxyapatite [Ca<sub>10</sub>(OH)<sub>2</sub>(PO<sub>4</sub>)<sub>6</sub>], often referred to as biological apatite. Solid state magnetic resonance (MR) spectroscopy evidence suggests that mature biological apatite may evolve from an initial precursor resembling dicalcium phosphate dihydrate (CaHPO<sub>4</sub>·2H<sub>2</sub>O, brushite), which is deposited in soft tissue

during the earliest stages of mineralization (29). Alternative models of vertebrate mineralization propose other precursors—such as amorphous calcium phosphate  $[Ca_3(PO4)_2]$  or octacalcium phosphate  $[Ca_8(HPO_4)_2(PO_4)_4\cdot 5H_2O]$ —that may also transform into mature apatite over time. Hydroxyapatite, containing unprotonated phosphate  $(PO_4^{-3})$ , and brushite, containing protonated phosphate  $(HPO_4^{-2})$ , have been used as chemical models for the respective unprotonated and protonated phosphate ions in biological calcification. Therefore, one measure of the maturity of the biological mineral may be obtained by assessing the relative concentrations of  $HPO_4^{-2}$  and  $PO_4^{-2}$ , given that mature bone mineral is dominated by  $PO_4^{-3}$  and has a lower  $HPO_4^{-2}$  concentration (29, 30).

Although several studies have characterized mineral phases in vascular calcification using techniques such as Fourier transform infrared spectroscopy (FTIR) and x-ray diffraction, these analyses have primarily provided qualitative identification of crystalline forms (e.g., hydroxyapatite, whitlockite) rather than quantitative differentiation of phosphate ion species. FTIR investigations by Rey et al. in bone (31, 32) and by Orzechowska et al. in calcified aortic valves (33) demonstrated valuable insight into phosphate protonation and carbonate substitution but required dehydrated, deproteinized specimens and did not resolve the relative abundance of  $HPO_4^{-2}$  and  $PO_4^{-3}$ in situ. In hydrated vascular tissues, conventional chemical analyses and vibrational spectroscopies remain limited by strong interference from residual water, proteins, and lipids (34). Clinical imaging modalities such as cardiac computed tomography (CT), intravascular ultrasound, and optical coherence tomography provide structural or qualitative compositional information but cannot assess mineral chemistry at the molecular level (35-41). In contrast, solid state MR spectroscopy offers a complementary approach capable of identifying and quantifying phosphate ion species in minimally processed mineralized tissues.

In this study, we employed two fundamental solid state MR spectroscopy techniques to analyze calcified tissue specimens: magic angle spinning (MAS) and cross-polarization (CP). The more common type of MR spectroscopy is performed on fluids, such as soft tissues *in vivo* or chemical solutions, where the signals from individual chemical groups (e.g., methyl groups, sodium ions, or water molecules) appear as resonance lines characterized primarily by their positions along the horizontal axis, known as the chemical shift, and measured in parts per million (ppm). Each chemical shift value uniquely corresponds

to the identity of the respective chemical group. In contrast to fluids, in which rapid molecular tumbling and diffusion occur, molecules within solids are fixed in positions and orientations, making their chemical shifts orientation Consequently, MR spectra of solid substances, such as calcium phosphate mineral crystals present in calcified tissues, exhibit broad resonance patterns spanning a wide frequency range, complicating direct identification of chemical groups from single-valued chemical shifts. Such broad resonance profiles, known as powder patterns, reflect the geometric symmetry of the chemical group or ion. The central position of the powder pattern corresponds to the isotropic chemical shift that would be observed if the molecules were freely mobile, as in a fluid state.

MAS facilitates MR spectroscopy of solids by rapidly rotating the specimen around an axis inclined at approximately 54.7 degrees relative to the external magnetic field, the so-called "magic angle" (42). Rapid rotation partially averages orientation-dependent chemical shifts, analogous to random molecular tumbling in liquids, significantly reducing the breadth of powder patterns toward narrower resonance lines. To achieve a single-valued chemical shift, rotation rates must surpass the intrinsic width of the powder pattern, a condition that is technically challenging. Typically, lower rotation rates result in partial narrowing, producing a pattern characterized by sidebands spaced at intervals equal to the rotation frequency (e.g., Figure 1).

CP serves two main functions in solid state MR spectroscopy. First, CP can enhance signals from nuclear isotopes with inherently low signal-to-noise ratio (SNR), such as those with low MR frequencies, low isotopic or chemical abundances, or long spin-lattice relaxation times T1. This enhancement is achieved by transferring magnetization from isotopes with higher SNR (commonly protons, <sup>1</sup>H) to the isotope of interest through simultaneous radiofrequency (RF) excitation. Second, CP is useful for spectral editing, differentiating chemical groups based on their proximity to the isotope source of magnetization. CP and MAS are frequently combined as cross-polarization magic angle spinning (CPMAS). It is important to note that CP magnetization transfer and the magnetization transfer effect in clinical MRI are fundamentally different. The former occurs via transverse magnetization exchange on microsecond-tomillisecond time scales, whereas the latter occurs on significantly longer (millisecond-to-second) time scales as a result of the diffusion of magnetization transported either by chemical diffusion of nuclear spins or by spin-spin coupling.

To date, aside from straightforward non-CP phosphorus-31 (<sup>31</sup>P) MAS measurements (43, 44), solid state MR techniques have not been utilized for examining vascular calcification. <sup>1</sup>H-<sup>31</sup>P solid state CPMAS MR spectroscopy has proven effective in quantifying bone mineral and solid organic matrix *ex vivo* (45–51). In biological specimens, distinguishing phosphate ions such as PO<sub>4</sub><sup>-3</sup> and HPO<sub>4</sub><sup>-2</sup> based on chemical shifts (3.1 ppm and 1.4 ppm, respectively) may be challenging, as inherent crystallographic disorder leads to broad resonance linewidths even with MAS. Thus, measurement of CP transfer rates depend strongly on the proton-phosphorus distances, and may help discriminate between these ions. For instance, rapid CP occurs in HPO<sub>4</sub><sup>-2</sup> ions in which <sup>1</sup>H and <sup>31</sup>P nuclei are spaced by

only a few tenths of a nanometer. Conversely, hydroxyapatite consists of spatially separated  $OH^-$  ions (protons) and  $PO_4^{-3}$  ions, leading to slower CP. Thus, the CP rate is reflective of the local crystal structure and can inform about the types of phosphate ions present, as established by prior studies in bone (47, 52). Indeed,  $^1H^{-31}P$  CPMAS investigations of progressively mineralizing embryonic to mature chicken bone have demonstrated a clear reduction in  $HPO_4^{-2}$  content from initial embryonic mineralization (approximately 8 days post-egg laying) to fully mature bone in 75-week-old chickens (30, 47). Given the biological parallels between bone mineralization and vascular calcification, we hypothesize that CPMAS could similarly reveal compositional variations within calcified vascular tissues, potentially providing insights into the mineral maturity of these tissues.

In this study, we applied CPMAS MR spectroscopy to investigate pathological calcifications from human plaque, human aortic valve, and the aorta of apolipoprotein E (ApoE)deficient mice, along with human trabecular bone specimens. To characterize mineral maturity, we compared these spectra to reference spectra of calcium phosphates commonly used as mineral models of biological calcification. CP transfer rates were derived to assess differences in crystal structure and composition. Additionally, we applied Herzfeld-Berger (HB) analysis (53) to extract the principal values of the chemical shift tensor (CST), parameters mathematically modelling the orientation-dependent variation in chemical shifts, from the spectral data. Given adequate spectral quality, indicated by clear identification and assignment of spinning sidebands to phosphate ions (PO<sub>4</sub><sup>-3</sup> and HPO<sub>4</sub><sup>-2</sup>), HB analysis can reliably determine both the relative abundance of these phosphate species and their respective chemical shift tensors, despite significant spectral overlap.

#### 2 Materials and methods

#### 2.1 Specimens

Commercial synthetic compounds included hydroxyapatite  $Ca_{10}(OH)_2(PO_4)_6$ , brushite (CaHPO<sub>4</sub>·2H<sub>2</sub>O), and monetite (CaHPO<sub>4</sub>) (Fisher Scientific, Hampton, NH, USA) were used without further purification or analysis. Human specimens included trabecular bone from autopsy (n=1), calcified aortic plaque (n=1) from autopsy, and calcified human aortic valves (n=5) acquired at the time of surgical excision and placed in neutral buffered formalin. Calcified aortic tissue (aortic root and arch vessels) was harvested *en bloc* from 60-week-old ApoE-deficient mice (n=1), that had been fed an atherogenic diet from 10 weeks of age; mouse specimens were preserved in formaldehyde buffer. All specimens were stored at  $-80^{\circ}$ C until MR scanning.

Prior to MR spectroscopy, intravital fluorescence microscopy of the carotid artery in these mice was performed using a bisphosphonate-derived imaging agent (OsteoSense 750; dose 2 nmol/150  $\mu L$ ).  $\mu CT$  of the mice was also performed to detect calcification. The human aortic plaque specimen was obtained

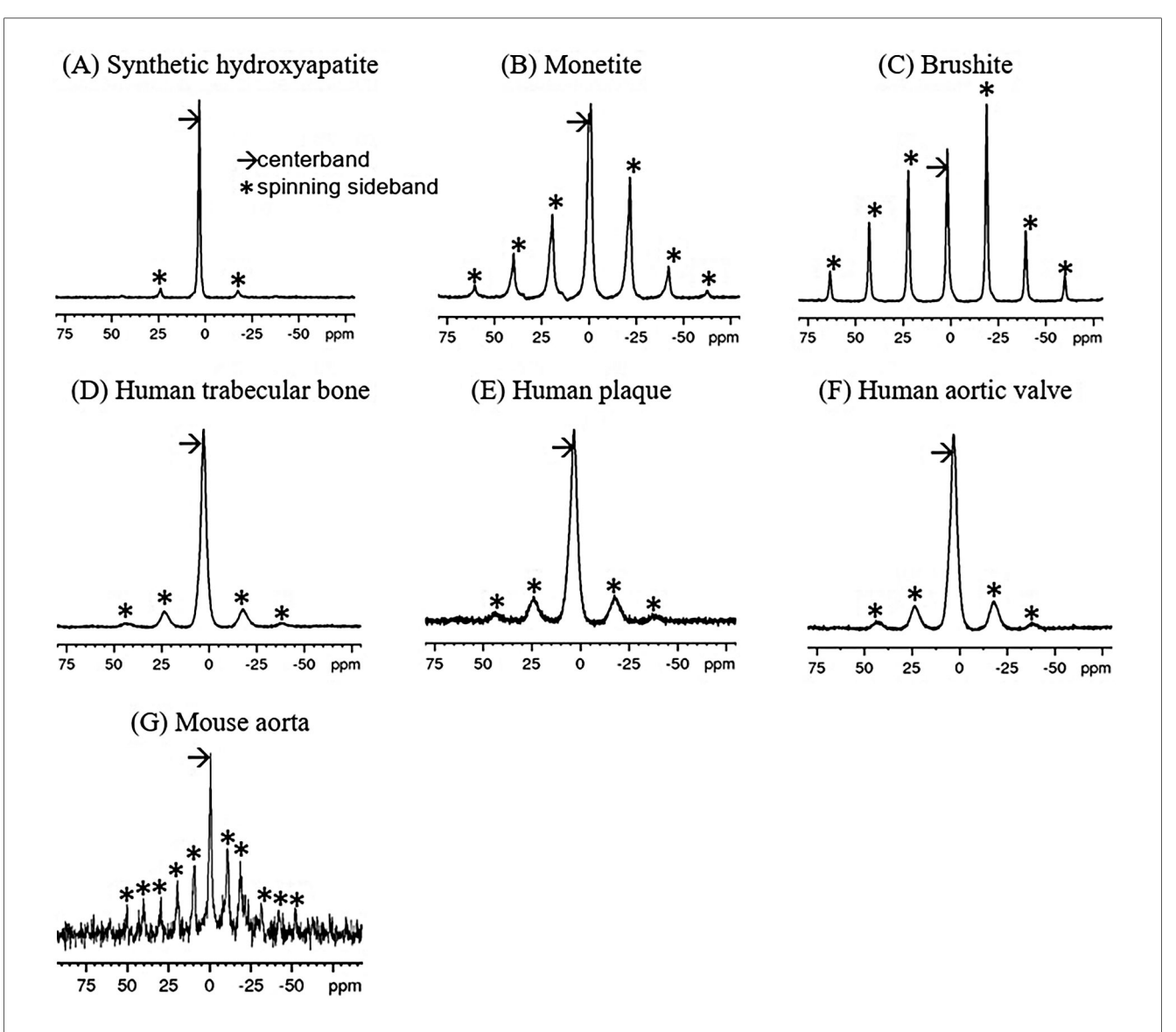


FIGURE 1  $^{31}\text{P}$  single-pulse MAS spectra of synthetic calcium phosphate compounds (A–C) and  $^{1}\text{H}-^{31}\text{P}$  CPMAS spectra of mineralized tissues (D–G). The spin rate for (A–F) was 5 kHz (~21 ppm), while that for (G) was 2.5 kHz (~10.5 ppm). Note that sidebands (\*) are spaced at the spin rate. Chemical shifts are referenced to 85%  $\text{H}_{3}\text{PO}_{4}$ .

from autopsy and consisted of a macroscopically calcified aortic segment from a donor with advanced atherosclerosis. Morphological classification (e.g., sheet-like vs. nodular) was not performed, as only a small portion of the calcified tissue was retained for spectroscopy, and no additional imaging or histological characterization was available.

Animal studies were approved by the respective Institutional Animal Care and Use Committees. Use of discarded human specimens was approved by the Massachusetts General Hospital Institutional Review Board.

#### 2.2 MR spectroscopy

Spectra were acquired using a Bruker Biospin (Billerica, MA, USA) Avance III multinuclear MR spectrometer equipped with

a 14 Tesla Magnex Scientific (Oxford, UK) wide bore magnet  $(f_{1H} = 600 \text{ MHz})$  and  $f_{31P} = 243 \text{ MHz}$ . Samples, compounds or calcified portions of the biological specimens, were tightly packed into 4 mm zirconia MAS rotors with a volume of about 78 μL. Both single-pulse <sup>31</sup>P MAS and <sup>1</sup>H-<sup>31</sup>P CPMAS spectra were acquired. For CP acquisitions, the 90° RF pulse length was 4.5 μs (B<sub>1</sub> field 55 kHz) on both <sup>1</sup>H and <sup>31</sup>P channels. Single-pulse <sup>31</sup>P spectra used a 90° RF pulse of 4.1 µs. The MAS spin rate was 5 kHz for most specimens, with 32 averages per spectrum and 2 s recycle delay (TR), resulting in 64 s acquisition duration per spectrum. For mouse aortic samples, which had lower mineral content and showed spinning instability due to tissue heterogeneity, the MAS rate was reduced to 2.5 kHz. To compensate, 7,400 scans were acquired per spectrum, giving a total acquisition time of approximately 4.1 h to ensure adequate signal-to-noise ratio (SNR). CP spectra were

also acquired with varying CP times to measure  $^{1}\text{H}^{-31}\text{P}$  CP time constants ( $\tau_{\text{CP}}$ ) and  $^{1}\text{H}$  rotating frame spin-lattice relaxation time constants ( $T_{1p}$ ) for the buildup and loss of magnetization, respectively.

#### 2.3 MR data analysis

Spectral data were processed offline using Bruker TopSpin 3.6.2 (Bruker, Billerica, MA, USA). Up to 2 ppm line broadening was applied to the mouse aorta spectra for reasonable SNR. For each series of CP spectra with varying CP times, the spectrum with the most intense centerband exhibited the highest SNR, and its phase correction was applied to all spectra in the series. Because it is typically not possible to use an internal chemical shift reference in solid state MR spectroscopy, a hydroxyapatite external reference set to 3.1 ppm (corresponding to 85% phosphoric acid defined as 0 ppm) was applied.

Herzfeld-Berger analysis was performed on the spectra used for phasing, employing the software tool ssNake (55) to extract the principle values of the CST. The principle values constitute a set of three numbers which can be mathematically expressed in multiple ways: as three principal values  $\delta_{11}$ ,  $\delta_{22}$ , and  $\delta_{33}$  where  $\delta_{11} \geq \delta_{22} \geq \delta_{33}$ , or as the isotropic chemical shift (analogous to the chemical shift in the fluid state)  $\delta_i$ , the total anisotropy  $\Delta$ , and the asymmetry parameter  $\eta$ .

The biological specimens generally exhibit spectra with broader linewidths than those of the synthetic compounds, such that the small isotropic chemical shift difference between  $PO_4^{-3}$  and  $HPO_4^{-2}$  prevents these resonances from being separately resolvable. For these spectra, the ssNake program fit the sideband pattern to two CSTs, putatively  $PO_4^{-3}$  and  $HPO_4^{-2}$ . The isotropic (liquid-state equivalent) chemical shift  $\delta_i$  is given by Equation 1:

$$\delta_i = \frac{1}{3}(\delta_{11} + \delta_{22} + \delta_{33}) \tag{1}$$

The total anisotropy  $\Delta$ , a measure of the overall width of the chemical shift powder pattern, can be calculated as Equation 2:

$$\Delta = \delta_{33} - \delta_{11} \tag{2}$$

This quantity provides an estimate of the extent to which the point symmetry of the crystal lattice at the nucleus deviates from ideal tetrahedral geometry. When the total anisotropy is zero, the spectral line appears sharp. The asymmetry parameter  $\eta$ , which quantifies the deviation of the chemical shift tensor from axial symmetry, is given by Equation 3:

$$\eta = \begin{cases}
\frac{\delta_{22} - \delta_{33}}{\delta_{11} - \delta_i} & \delta_i \ge \delta_{22} \\
\frac{\delta_{22} - \delta_{11}}{\delta_{33} - \delta_i} & \delta_i \le \delta_{22}
\end{cases}$$
(3)

Centerband peak areas were determined by integration to quantify signal intensity s(t) for extracting CP and rotating frame spin-lattice relaxation  $(T_{1p})$  time constants as a function of CP contact time t. The signal was fit to Equation (4) using a nonlinear least squares approach:

$$s(t) = M_0 \left( 1 - e^{-\frac{t}{\tau_{CP}}} \right) e^{-\frac{t}{T_{1\rho}}}$$
 (4)

The analysis models the signal as a composite of contributions from both  $PO_4^{-3}$  and  $HPO_4^{-2}$  ions, without attempting to resolve them separately. The rationale behind this model for the time dependence of the  $^{31}P$  signal is that the first exponential term describes the buildup of magnetization via rapid  $^{1}H$  to  $^{31}P$  polarization transfer, while the second exponential term accounts for signal decay due to relaxation in the proton rotating frame. Additional details are provided in the discussion section.

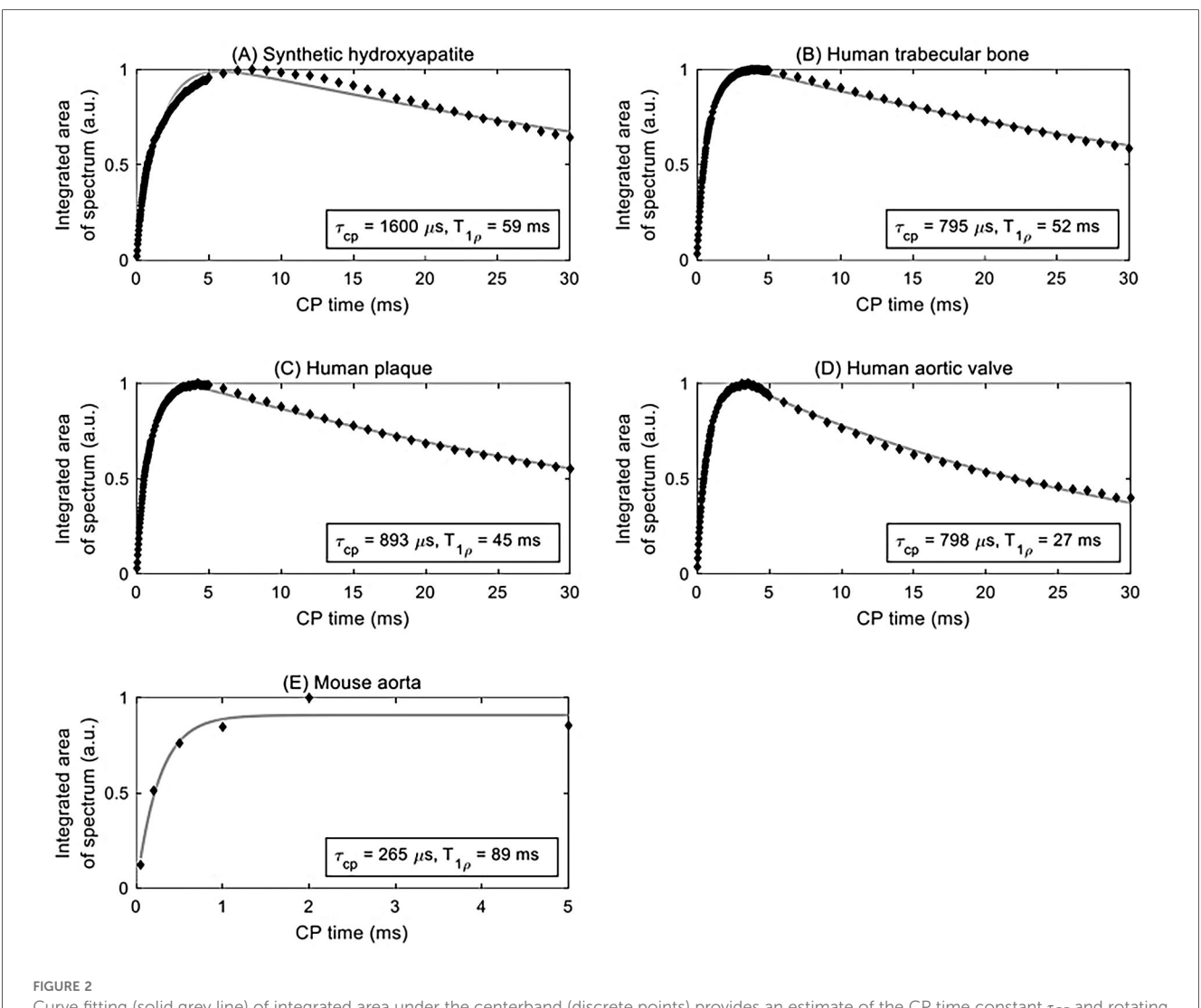
## 3 Results

# 3.1 <sup>31</sup>P MR spectra

<sup>31</sup>P MAS spectra of the synthetic calcium phosphates and <sup>1</sup>H-<sup>31</sup>P CPMAS spectra biological specimens are shown in Figure 1. Because of the high point symmetry of the unprotonated phosphate in hydroxyapatite (Figure 1A), its chemical shift anisotropy is small, and the spinning sidebands are weak. Its centerband (isotropic chemical shift) occurs at 3.1 ppm. There is no indication of other types of phosphate ion in the spectrum. In contrast, monetite (Figure 1B) and brushite (Figure 1C) contain a single acidic phosphate HPO<sub>4</sub><sup>-2</sup> and no PO<sub>4</sub><sup>-3</sup>. The lower symmetry of the HPO<sub>4</sub><sup>-2</sup> ion in these compounds results in a large chemical shift anisotropy and a prominent sideband pattern. Their isotropic shifts occur upfield from hydroxyapatite.

The biological specimens exhibit broader spectral linewidths than the synthetic materials. The bone, plaque and calcified valve spectra (Figures 1D-F) resemble that of hydroxyapatite and have isotropic shifts of 3.1 ppm, but with somewhat more prominent sideband patterns similar to monetite and brushite. This suggests that the predominant phosphate ion is  $PO_4^{-3}$ , and that it is accompanied by a small amount of  $HPO_4^{-2}$  which is contributing to the sidebands.

The mouse aorta spectrum is distinctly different from those of the other biological specimens in that the sidebands are more prominent, suggesting a higher level of  $\mathrm{HPO_4^{-2}}$  content (Figure 1G). The lower spin rate and SNR make visual comparison with the other spectra difficult. However, the analyses below reveal distinct differences from the other biological specimens.



Curve fitting (solid grey line) of integrated area under the centerband (discrete points) provides an estimate of the CP time constant  $\tau_{CP}$  and rotating frame spin-lattice relaxation time constant  $T_{1p}$  for various samples: (A) synthetic hydroxyapatite, (B) human trabecular bone, (C) human plaque, (D) human aortic valve, and (E) mouse aorta.

# 3.2 Time constants

Signal curves as a function of CP time of selected specimens are shown in Figure 2, and the corresponding numerical results of the fits are summarized in Table 1. The time axis for the mouse aorta spectrum is limited to 5 ms because of challenges with spinning stability; this  $T_{1p}$  value therefore has higher uncertainty. All fits converged successfully.

Hydroxyapatite, containing only unprotonated phosphate, was found to have the longest CP time constant at 1,600  $\mu s$ . For comparison, brushite, containing only protonated phosphate, was found in a previous study (47) to have a CP time constant of 140  $\mu s$ . The biological specimens in this study fall in between these two extremes. The human specimens tend to be in the range of 700–900  $\mu s$ , whereas the mouse aorta specimen has a much shorter CP time constant of about 270  $\mu s$ , much closer to that of brushite.

TABLE 1 Time constants derived from the double-exponential model of CPMAS signal evolution.

Specimen	$ au_{\mathit{CP}}(\mu s)^{a}$	$T_{1\rho}(\mathrm{ms})^{a}$	R-squared	
Hydroxyapatite	1,600 ± 77	59 ± 7	0.957	
Human trabecular bone	795 ± 14	52 ± 2	0.997	
Human plaque	893 ± 22	45 ± 2	0.995	
Human aortic valve #1	820 ± 25	56 ± 4	0.998	
Human aortic valve #2	733 ± 21	81 ± 12	0.998	
Human aortic valve #3	$760 \pm 30$	22 ± 1	0.989	
Human aortic valve #4	$684 \pm 10$	36 ± 1	0.997	
Human aortic valve #5	798 ± 10	27 ± 1	0.997	
Mouse aorta <sup>b</sup>	265 ± 133	89 ± 50	0.974	

 $^{\mathrm{a}}\mathrm{Values}$  are mean  $\pm$  variance. The variance indicates 95% confidence bounds computed using the inverse of Student's t cumulative distribution function and the estimated covariance matrix of the coefficient estimates.

 $^{\rm b}{\rm Reduced}$  accuracy due to low SNR and insufficient measurement time for  $T_{1\rho}$  quantification.

#### 3.3 Herzfeld-Berger chemical shift tensor

Chemical shift parameters based on Herzfeld-Berger analysis of the spinning sideband patterns are reported in Table 2. The isotropic chemical shifts  $\delta_i$  are estimated to be accurate to  $\pm 0.2$  ppm, and the chemical shift anisotropies  $\Delta$  are estimated to be accurate to  $\pm 2$  ppm. The asymmetry parameters  $\eta$  are estimated to be accurate to  $\pm 0.05$ . The sideband patterns of the synthetic compounds were fit to a single CST, whereas those of the biological specimens were fit to two CSTs, permitting the separation of unprotonated from protonated phosphates.

The  $^{31}P$  chemical shift anisotropy of hydroxyapatite ( $\Delta=19~\text{ppm}$ ) is small as expected because  $PO_4^{-3}$  in hydroxyapatite is located at site of high tetrahedral symmetry. Brushite, which contains a single protonated phosphate ion  $HPO_4^{-2}$ , possesses a lower point symmetry, and therefore a larger chemical shift anisotropy ( $\Delta=125~\text{ppm}$ ) than hydroxyapatite. The isotropic shift  $\delta_i$  of brushite is shifted upfield (less positive) from hydroxyapatite, similar to the upfield shift with decreasing pH (increased protonation) found in aqueous orthophosphates (56, 57). The large value of  $\eta$  from brushite indicates a nearly equidistant separation of the principal values of the tensor, and a highly symmetric powder pattern. The  $\delta_i$  of monetite (CaHPO<sub>4</sub>, the anhydrous form of brushite), lies even further upfield.

Distinct from the "pure" environment of PO<sub>4</sub><sup>-3</sup> or HPO<sub>4</sub><sup>-2</sup> in the synthetic salts, biological calcium phosphates are mixed crystals containing both types of phosphate ions, as established by indirect wet chemical evidence (58, 59). Biological calcium phosphates also contain miscellaneous crystal lattice defects, vacancies and substitutions. The high surface area of biological calcium phosphate nanocrystals also substantially increases the microscopic heterogeneity of phosphate chemical environments. All of these factors increase the <sup>31</sup>P spectral linewidths as readily

TABLE 2  $^{31}\mbox{P}$  chemical shift tensor parameters of synthetic and biological calcium phosphate compounds.

Specimen	Experiment	$\sigma_i$ (ppm)	$\Delta$ (ppm)	η
Hydroxyapatite	CP	3.2	19	0.46
Brushite	CP	1.7	125	0.94
Monetite	CP	-0.9	77	0.98
Human trabecular bone	CP—tensor 1	3.2	25	0.11
	CP—tensor 2	3.1	32	0.61
Human plaque	CP—tensor 1	3.2	30	0.15
	CP—tensor 2	3.0	48	0.90
Human aortic valve #1	CP—tensor 1	3.2	26	0.83
	CP—tensor 2	2.9	61	0.92
Human aortic valve #2	CP—tensor 1	3.2	27	-0.32
	CP—tensor 2	1.4	78	0.98
Human aortic valve #3	CP—tensor 1	3.1	19	0.39
	CP—tensor 2	3.0	90	0.98
Human aortic valve #4	CP—tensor 1	3.1	19	0.39
	CP—tensor 2	3.0	90	0.98
Human aortic valve #5	CP—tensor 1	3.1	21	0.38
	CP—tensor 2	2.9	78	0.79
Mouse aorta	CP—tensor 1	3.1	43	0.72
	CP—tensor 2	-5.2	48	0.36

apparent from the spectra in Figures 1D-G. Therefore, the analysis of the biological specimens parametrized the spectra as containing contributions from two chemical shift tensors representing PO<sub>4</sub><sup>-3</sup> and HPO<sub>4</sub><sup>-2</sup>. Because HPO<sub>4</sub><sup>-2</sup> is the minor component, and because the PO<sub>4</sub><sup>-3</sup> and HPO<sub>4</sub><sup>-2</sup> spectra overlap almost perfectly, a lower accuracy is expected in the HPO<sub>4</sub><sup>-2</sup> parameters resulting from the fit. The isotropic chemical shift  $\delta_i$ calculated from the first tensor of human trabecular bone, plaque and human aortic valves are all at 3.2 ppm (±0.2 ppm), which can be assigned to unprotonated phosphate based on its similarity to the hydroxyapatite isotropic shift. The chemical shift anisotropies  $\Delta$  calculated for the first tensor of the human specimens are somewhat larger than that of hydroxyapatite. The larger values are likely a reflection of the disordered nature of biological calcium phosphate crystals. The second tensor exhibits isotropic chemical shifts also at 3.2 ppm (±0.2 ppm), except for human aortic valve specimen #2 for which  $\sigma_i = 1.4$  ppm. The chemical shift anisotropy derived from the second tensor of the human specimens is increased as compared to those of the first tensor, suggestive of some level of "brushite-like" ions in the mineral crystals. The mouse aorta specimen exhibits a spectrum with considerable differences from the other biological specimens. One of the isotropic chemical shifts of mouse aorta lie substantially upfield ( $\sigma_i = -5.2 \text{ ppm}$ ), implying a higher HPO<sub>4</sub><sup>-2</sup> content of the crystals. This was further supported by the increased sideband intensities in Figure 1G. Furthermore, an earlier study reported  $HPO_4^{-2}$  anisotropy  $\Delta = 116$  ppm and  $\eta = 1$  of a few bone specimens from chick embryo, adult chicken, calf embryo, adult calf, rabbit embryo and adult rabbit (47), which are consistently close to values of brushite.

The calculated chemical shift tensors can be used to generate simulated spinning patterns that closely resemble the original spinning patterns, as shown in Figure 3. For biological specimens characterized by two tensors, the composite pattern is the sum of two simulated patterns. The pattern with a stronger centerband and resonance closer to 3.1 ppm (green traces in Figures 3C-F) is associated with unprotonated phosphates, whereas the pattern with a weaker and broader centerband and resonance shifted upfield (less positive, blue traces in Figures 3C-F) is associated with protonated phosphates. Fitting the mouse spectrum to one tensor gives a reasonable result. The spectrum is too noisy to fit two tensors with reasonable confidence. However, the mouse spectrum implies the presence of freshly deposited mineral crystals as opposed to entirely mature hydroxyapatite crystals in the calcification of mouse aorta.

#### 4 Discussion

The CP rate depends strongly on the direct dipole-dipole coupling between  $^{1}\text{H}$  and  $^{31}\text{P}$  nuclei. This rate varies as the inverse sixth power of the internuclear distance and can therefore be used to discriminate between calcium phosphates with close vs. more distant  $^{31}\text{P}^{-1}\text{H}$  spacing, as well as deduce general information reflective of the crystal geometry about the phosphate ion.  $\tau_{cp}$  also depends on the number of coupled

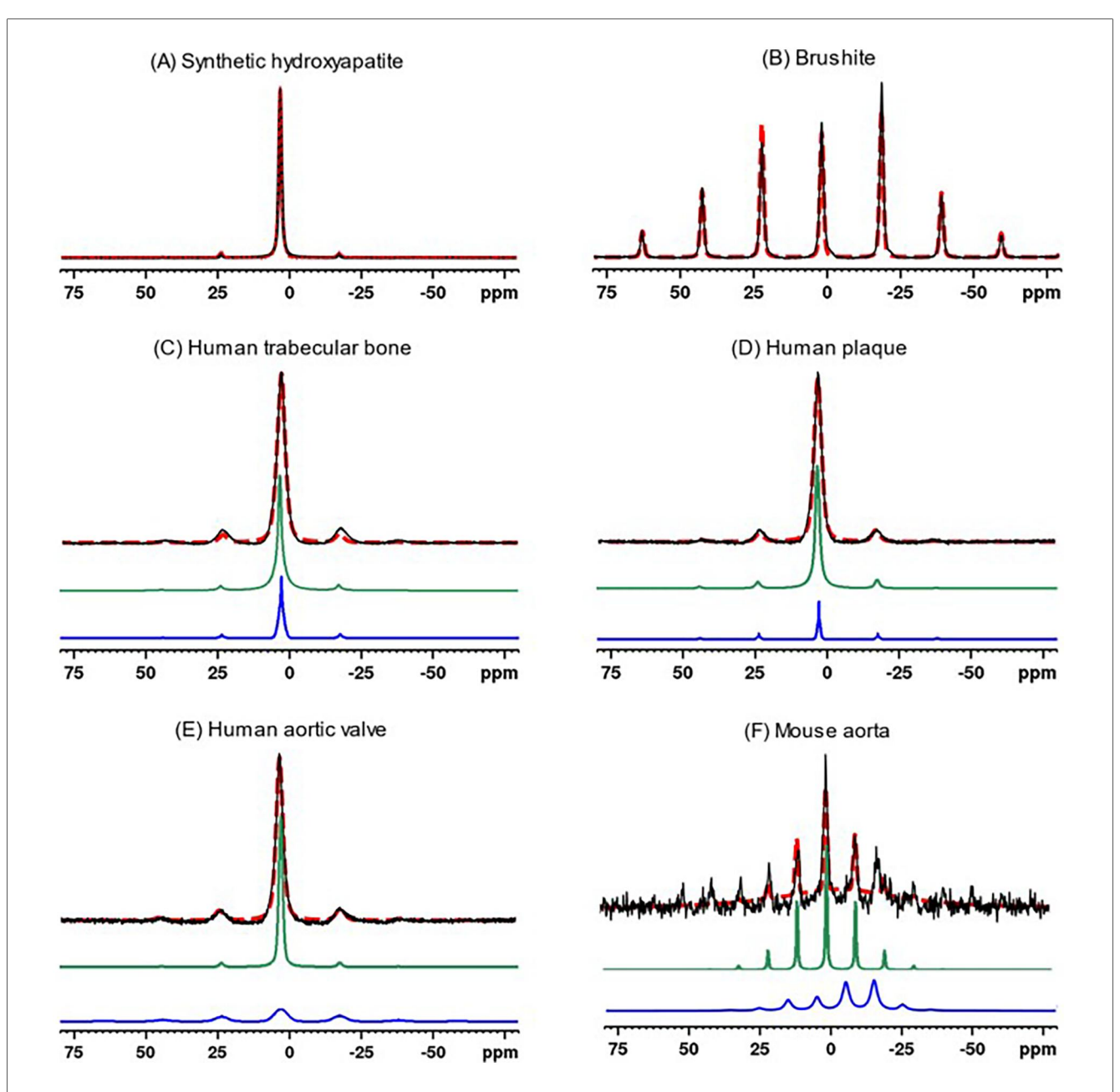


FIGURE 3

31-P MAS experimental spectra (solid black traces) of synthetic calcium phosphate compounds and biological specimens, and corresponding simulated spectra (red dashed traces) based on Herzfeld-Berger chemical shift tensor analysis. The synthetic compound spectra were fit to a single tensor, whereas biological specimens were fit to two tensors (individual simulated tensor spectra displayed as green and blue traces). The latter composite simulated spectra (red dashed traces) are the sums of the spectra from the two components. (A) Synthetic hydroxyapatite, (B) Brushite, (C) Human trabecular bone, (D) Human plaque, (E) Human aortic valve, (F) Mouse aorta.

spins.  $^{31}P$  in  $HPO_4^{-2}$  transfers magnetization with  $^{1}H$  at a rapid rate because the participating nuclei are within the same ion and are in close proximity. At the other end of the scale,  $PO_4^{-3}$  in hydroxyapatite transfers magnetization far more slowly because the closest protons are located in other, more distant, ions (e.g.,  $OH^-$  or  $HPO_4^{-2}$ ) in the crystal lattice. In this case,  $^{31}P$  signals from nuclei separated from protons by more than a few tens of a nm, such as the distance between phosphate ions in calcium phosphate crystals and the protons in surrounding tissue and matrix, are fully suppressed.

 $T_{1\rho}$  is the relaxation time constant for energy exchange between nuclear spins and the lattice, measured in the rotating frame of reference. It is analogous to the more familiar spin-lattice relaxation time constant  $T_1$ .  $T_1$  is sensitive to molecular motions with correlation times comparable to the inverse of the Larmor frequency. For example, for a proton Larmor frequency of 600 MHz ( $B_0 \sim 14$  T), the proton  $T_1$  is determined by molecular motion correlation times on the order of ns. A substantial degree of molecular motion (molecular tumbling or diffusion, chemical exchange, or even spin exchange)

occurring at this rate will contribute to a shortening in the  $T_1$  value. Because  $T_{1\rho}$  is measured in the rotating reference frame with respect to a spinlock RF field on the order of millitesla  $(v_1 \sim \text{kHz})$  rather than Tesla  $(v_0 \sim \text{tens}$  to hundreds of MHz), it is sensitive to relatively slow molecular motions (e.g., motions of macromolecules, or slow spin exchange characteristic of substances with dilute, widely spaced, protons).

Spin-lattice relaxation of either type  $(T_{1\rho} \text{ or } T_1)$  is mediated by the time-dependence (e.g., vibrations and motions of surrounding atoms and molecules) of the spin-spin coupling interaction (60). Since protons have a much stronger magnetic moment than phosphorus nuclei, they play the dominant role in spin-lattice relaxation. <sup>31</sup>P nuclei therefore tend to undergo spin-lattice relaxation via spin-spin coupling to the proton "reservoir" (the collective assembly of protons in the crystal lattice, water molecules, bone matrix, etc.). Therefore, variations in  $T_{1\rho}$  may be indicative of water content, presence of protons in the crystal lattice, and similar aspects of the chemical environment. However, there are no clear trends in the  $T_{1\rho}$  data for the specimens studied here.

The spectra of all the human specimens resemble that of hydroxyapatite, except the human specimens exhibit more prominent sidebands, as does that of the mouse aorta. As found in earlier studies of animal bone, this is generally the case for mature bone mineral, which is primarily apatitic with a small content of  $HPO_4^{-2}$  that contributes to the sidebands (45, 47). In contrast, calcification in the ApoE-deficient mouse resembled that of immature or embryonic bone. Moreover, calcified mouse aorta exhibits much shorter CP time constants, implying a higher content of HPO<sub>4</sub><sup>-2</sup> in the calcium phosphate crystals. Prior studies detected the presence of microcalcifications (1 µm-30 µm) in the aorta of ApoE-deficient mice fed a high cholesterol diet for as early as 12 weeks starting at 8-10 weeks of age (61, 62) using molecular imaging and microscopy. Despite the age of the ApoE-deficient mouse (60 weeks) in this study, its calcification did not resemble that observed in vascular calcification in humans. This result could be because calcification in humans may evolve over many years, far longer than the 60 weeks in the mice. Therefore, the use of mouse models for human calcified tissues should be viewed with the caveat that there may be fundamental differences between human and mouse calcification due to the very different time scales for the deposition and remodeling of the calcium phosphate crystals. This may in part explain the discrepancy in the response to statin therapy, which has been effective in ApoE-deficient mice (63-65) but exhibited controversial effects in human patients with atherosclerosis plaques (66-71). Calcification in the aged ApoE-deficient mouse thus likely models early preclinical calcification in human aortic valves (72), but not the mature pattern of calcification seen in patients with established aortic stenosis.

The small tissue size and relatively low mineral density of murine aortic calcifications constrain the signal-to-noise ratio attainable in solid state <sup>1</sup>H-<sup>31</sup>P MR spectroscopy, limiting the feasibility of analyzing multiple age groups or lesion sizes within this dataset. Consequently, while the present findings clearly

demonstrate compositional differences between human and murine calcifications, we cannot fully exclude the contribution of mineral age or lesion maturity to the observed variation. Future studies incorporating ApoE-deficient mice at different ages and comparing larger and smaller plaques within the same animal will be important to distinguish the relative influence of mineral age, lesion progression, and intrinsic compositional factors.

In addition to mineral age, crystal size and surface chemistry may also influence the apparent phosphate speciation (73). Biological apatite crystals are typically nanometer-scale platelets (e.g., 15-100 nm length, 0.5-4 nm in thickness) and are often coated by a hydrated, disordered surface layer (74) that contains labile ions and is prone to ionic exchange (75). Solid state MR spectroscopy studies have shown that HPO<sub>4</sub><sup>2-</sup> ions are disproportionately localized in these amorphous surface layers — for example, Von Euw et al. (76) estimated a ~0.8 nm surface shell rich in protonated phosphate even on small particles. TEM imaging of synthetic apatite also reveals 1-2 nm amorphous surface layers (77). Because the surface-to-volume ratio is much higher in small crystals, a greater fraction of total phosphate may be in protonated form (HPO<sub>4</sub><sup>2-</sup>) relative to PO<sub>4</sub><sup>3-</sup>. Thus, the higher relative HPO<sub>4</sub><sup>2-</sup> content observed in mouse vs. human calcifications could partially reflect smaller, less-coalesced nanocrystals rather than purely younger mineral age.

Beyond nanoscale effects, variations in the extracellular environment can further modulate phosphate chemistry. During physiological bone mineralization, extracellular pH remains close to neutral, favoring  $PO_4^{-3}$ -rich apatite (78). In contrast, plaque microenvironments are often mildly acidic due to inflammation and hypoxia (79–81), which could shift the equilibrium toward protonated phosphate (HPO $_4^{-2}$ ). Variations in local pH, therefore, may contribute to the compositional differences observed between vascular and skeletal mineral.

A previous study (47) examining the spectrum of Ca (H<sub>2</sub>PO<sub>4</sub>)<sub>2</sub>·H<sub>2</sub>O has ruled out the possibility of the sideband patterns observed in biological calcium phosphates being associated with the protonated phosphate ion H<sub>2</sub>PO<sub>4</sub>-. The chemical shift anisotropy of Ca(H<sub>2</sub>PO<sub>4</sub>)<sub>2</sub>·H<sub>2</sub>O is much smaller than those of the biological specimens. Additionally, it is unlikely that there is a significant H<sub>2</sub>PO<sub>4</sub> content in biological calcium phosphates because an unusually acidic cellular environment would be required to maintain a substantial amount of H<sub>2</sub>PO<sub>4</sub> in vivo. Therefore, it was assumed that only two phosphate ions (PO<sub>4</sub><sup>-3</sup> and HPO<sub>4</sub><sup>-2</sup>) contribute to the spectra. In principle, each sideband pattern is affected by not only the <sup>31</sup>P chemical shift anisotropy, but also <sup>1</sup>H-<sup>31</sup>P and <sup>31</sup>P-<sup>31</sup>P dipolar interactions. However, these secondary effects are expected to be relatively minor under conditions of high magnetic field strength and 5 kHz magic angle spinning.

The goal of this study was to provide fundamental insights into the structure of calcified cardiovascular tissues but translational parallels that merit exploration may exist. Cardiovascular MRI in humans is being increasingly explored on 0.5 Tesla commercial systems (82, 83) and the relaxation frequency governing  $T_1$  exchange at this field is not that

different from  $T_{1\rho}$  at 14T (~36× with the 55 kHz  $B_1$  field used here). Moreover, portable MRI systems (Hyperfine Inc) operating in the low milli-Tesla range have been FDA-approved for point-of-care neuroimaging and  $T_1$  of carotid plaque on these systems would involve a relaxation frequency very similar to  $T_{1\rho}$  at 14T. These low field systems are based on proton MRI, and the lower polarization of <sup>31</sup>P would undoubtedly be challenging. However, hyperpolarization of <sup>31</sup>P in aqueous solution has been described (84) and may be able to mitigate the low SNR of organic phosphates in atherosclerotic plaque. While spatial resolution and SNR are indeed limited in low-field MRI, some valuable insights may be able to be obtained by comparing *in vivo*  $T_1$  measurements on low field systems with  $T_{1\rho}$  measurements *ex vivo* at 14T.

In addition to broader methodological extensions, future studies could perform solid state <sup>1</sup>H-<sup>31</sup>P MR spectroscopy on calcified tissues dissected from different regions within the same plaque or from plaques at distinct anatomical locations. Such site-specific spectroscopy would allow for comparison of mineral phase composition and maturity microenvironments that vary in cellular activity, lipid accumulation, or inflammatory state (85). In the present study, detailed morphological characterization of the calcified plaque specimen (e.g., nodular vs. sheet-like) was not available due to limited tissue availability and absence of complementary imaging. When combined with histological and microscopic analyses in future work, this spectroscopyapproach could offer a spatially understanding of mineral heterogeneity within human plaques and clarify how phosphate speciation relates to local biological processes such as inflammation, lipid deposition, and necrosis.

### 5 Conclusions

Solid state MR spectroscopy adds another dimension to the study of pathologic calcification. It provides a means to identify the presence of various phosphate ions in the calcium phosphate mineral. Human trabecular bone, calcified atherosclerotic plaque, and calcified aortic valve specimens were found to have similar CPMAS spectra, whereas the spectra of experimentally induced calcified mouse aortic calcification are somewhat different and suggestive of immature, recently deposited bone. Although solid state MR spectroscopy has been used to study bone in several contexts, it has rarely been applied to pathological ectopic calcification. While this methodology is not directly applicable to clinical use, it could be an important complement to basic studies of pathological calcification in atherosclerosis and related calcific disorders.

# Data availability statement

The raw data supporting the conclusions of this article will be made available by the authors, without undue reservation.

#### **Ethics statement**

The studies involving humans were approved by Massachusetts General Hospital. The studies were conducted in accordance with the local legislation and institutional requirements. The participants provided their written informed consent to participate in this study. The animal study was approved by Brigham and Women's Hospital Institutional Review Board. The study was conducted in accordance with the local legislation and institutional requirements.

#### **Author contributions**

Data curation, Formal analysis, Investigation, Methodology, Project administration, Software, Validation, Visualization, Writing - original draft, Writing - review & editing. CF: Data curation, Investigation, Methodology, Software, Supervision, Writing - original draft, Writing - review & Conceptualization, Funding acquisition, editing. EA: Investigation, Methodology, Resources, Supervision, Writing review Writing & editing. original draft, Conceptualization, Funding acquisition, Investigation, Methodology, Resources, Supervision, Writing - original draft, Writing - review & editing. BM: Data curation, Methodology, Resources, Writing - original draft, Writing - review & editing. AK: Formal analysis, Software, Validation, Writing - original draft, Writing - review & editing. JA: Conceptualization, Formal analysis, Funding acquisition, Investigation, Methodology, Resources, Supervision, Validation, Writing - original draft, Writing - review & editing.

# Funding

The author(s) declare financial support was received for the research and/or publication of this article. EA: NIH R01HL174066, the Leducq Foundation PRIMA network, and a research grant from Pfizer. BM: NIH T32HL007208 (DES). Martinos Center 14T MR spectrometer facility: NIH S10RR013026, S10OD023406, and S10OD038220. JY and JA: NIH R01AR075077 (grant R01EB029818).

# Acknowledgments

This has been released as a preprint at medRxiv (54).

#### Conflict of interest

The authors declare that the research was conducted in the absence of any commercial or financial relationships that could be construed as a potential conflict of interest.

The author(s) declared that they were an editorial board member of Frontiers, at the time of submission. This had no impact on the peer review process and the final decision. ensure accuracy, including review by the authors wherever possible. If you identify any issues, please contact us.

#### Generative AI statement

The author(s) declare that no Generative AI was used in the creation of this manuscript.

Any alternative text (alt text) provided alongside figures in this article has been generated by Frontiers with the support of artificial intelligence and reasonable efforts have been made to

### Publisher's note

All claims expressed in this article are solely those of the authors and do not necessarily represent those of their affiliated organizations, or those of the publisher, the editors and the reviewers. Any product that may be evaluated in this article, or claim that may be made by its manufacturer, is not guaranteed or endorsed by the publisher.

#### References

- 1. Bostrom K. Insights into the mechanism of vascular calcification. Am J Cardiol. (2001) 88(2A):20E-2E. doi: 10.1016/s0002-9149(01)01718-0
- 2. Shioi A, Mori K, Jono S, Wakikawa T, Hiura Y, Koyama H, et al. Mechanism of atherosclerotic calcification. *Z Kardiol.* (2000) 89(Suppl 2):75–9. doi: 10.1007/s003920070103
- 3. Epple M, Lanzer P. How much interdisciplinarity is required to understand vascular calcifications? Formulation of four basic principles of vascular calcification. Z Kardiol. (2001) 90(Suppl 3):2–5. doi: 10.1007/s003920170036
- 4. LeGeros RZ. Formation and transformation of calcium phosphates: relevance to vascular calcification. Z Kardiol. (2001) 90(Suppl 3):116–24. doi: 10.1007/s003920170032
- 5. Tomazic BB. Physiochemical principles of cardiovascular calcification.  $Z\ Kardiol.$  (2001) 90(Suppl 3):68–80. doi: 10.1007/s003920170046
- 6. Peters F, Epple M. Simulating arterial wall calcification in vitro: biomimetic crystallization of calcium phosphates under controlled conditions. Z Kardiol. (2001) 90(Suppl 3):81–5. doi: 10.1007/pl00022850
- 7. Wada T, McKee MD, Steitz S, Giachelli CM. Calcification of vascular smooth muscle cell cultures: inhibition by osteopontin. *Circ Res.* (1999) 84(2):166–78. doi: 10.1161/01.res.84.2.166
- 8. Jono S, McKee MD, Murry CE, Shioi A, Nishizawa Y, Mori K, et al. Phosphate regulation of vascular smooth muscle cell calcification. *Circ Res.* (2000) 87(7):E10–7. doi: 10.1161/01.res.87.7.e10
- 9. Fitzpatrick LA, Turner RT, Ritman ER. Endochondral bone formation in the heart: a possible mechanism of coronary calcification. *Endocrinology.* (2003) 144(6):2214–9. doi: 10.1210/en.2002-0170
- 10. Goldring SR. Inflammatory mediators as essential elements in bone remodeling. *Calcif Tissue Int.* (2003) 73(2):97–100. doi: 10.1007/s00223-002-1049-y
- 11. Doherty TM, Uzui H, Fitzpatrick LA, Tripathi PV, Dunstan CR, Asotra K, et al. Rationale for the role of osteoclast-like cells in arterial calcification. *FASEB J.* (2002) 16(6):577–82. doi: 10.1096/fj.01-0898hyp
- 12. Lampropoulos CE, Papaioannou I, Cruz DP. Osteoporosis-a risk factor for cardiovascular disease? *Nat Rev Rheumatol.* (2012) 8(10):587-98. doi: 10.1038/nrrheum.2012.120
- 13. Caffarelli C, Montagnani A, Nuti R, Gonnelli S. Bisphosphonates, atherosclerosis and vascular calcification: update and systematic review of clinical studies. *Clin Interv Aging*. (2017) 12:1819–28. doi: 10.2147/CIA.S138002
- 14. Santos LL, Cavalcanti TB, Bandeira FA. Vascular effects of bisphosphonates-a systematic review. *Clin Med Insights Endocrinol Diabetes*. (2012) 5:47–54. doi: 10. 4137/CMED.S10007
- 15. Ylitalo R. Bisphosphonates and atherosclerosis. Gen Pharmacol. (2000)  $35(6):287-96.\ doi: 10.1016/s0306-3623(01)00121-5$
- 16. Recker RR, Lewiecki EM, Miller PD, Reiffel J. Safety of bisphosphonates in the treatment of osteoporosis. *Am J Med.* (2009) 122(2 Suppl):S22–32. doi: 10.1016/j. amjmed.2008.12.004
- 17. Rodan GA, Fleisch HA. Bisphosphonates: mechanisms of action. J Clin Invest. (1996) 97(12):2692–6. doi: 10.1172/jci118722
- 18. Bakhshian Nik A, Hutcheson JD, Aikawa E. Extracellular vesicles as mediators of cardiovascular calcification. *Front Cardiovasc Med.* (2017) 4:78. doi: 10.3389/fcvm. 2017.00078
- 19. Burnett JR, Vasikaran SD. Cardiovascular disease and osteoporosis: is there a link between lipids and bone? *Ann Clin Biochem.* (2002) 39(Pt 3):203–10. doi: 10. 1258/0004563021902134

- 20. Christian RC, Harrington S, Edwards WD, Oberg AL, Fitzpatrick LA. Estrogen status correlates with the calcium content of coronary atherosclerotic plaques in women. *J Clin Endocrinol Metab.* (2002) 87(3):1062–7. doi: 10.1210/jcem.87.3.8354
- 21. Kiel DP, Kauppila LI, Cupples LA, Hannan MT, Donnell O, Wilson CJ, et al. Bone loss and the progression of abdominal aortic calcification over a 25 year period: the framingham heart study. *Calcif Tissue Int.* (2001) 68(5):271–6. doi: 10.1007/BF00.390833
- 22. Vliegenthart R, Oudkerk M, Hofman A, Oei H-HS, van Dijck W, van Rooij FJA, et al. Coronary calcification improves cardiovascular risk prediction in the elderly. *Circulation*. (2005) 112:572–7. doi: 10.1161/CIRCULATIONAHA.104.488916
- 23. Martin SS, Blaha MJ, Blankstein R, Agatston A, Rivera JJ, Virani SS, et al. Dyslipidemia, coronary artery calcium, and incident atherosclerotic cardiovascular disease: implications for statin therapy from the multi-ethnic study of atherosclerosis. *Circulation*. (2014) 129(1):77–86. doi: 10.1161/circulationaha.113. 003625
- 24. Ferencik M, Schlett CL, Ghoshhajra BB, Kriegel MF, Joshi SB, Maurovich-Horvat P, et al. A computed tomography-based coronary lesion score to predict acute coronary syndrome among patients with acute chest pain and significant coronary stenosis on coronary computed tomographic angiogram. *Am J Cardiol.* (2012) 110(2):183–9. doi: 10.1016/j.amjcard.2012.02.066
- 25. Ehara S, Kobayashi Y, Yoshiyama M, Shimada K, Shimada Y, Fukuda D, et al. Spotty calcification typifies the culprit plaque in patients with acute myocardial infarction: an intravascular ultrasound study. *Circulation*. (2004) 110(22):3424–9. doi: 10.1161/01.Cir.0000148131.41425.E9
- 26. Criqui MH, Denenberg JO, Ix JH, McClelland RL, Wassel CL, Rifkin DE, et al. Calcium density of coronary artery plaque and risk of incident cardiovascular events. *JAMA*. (2014) 311(3):271–8. doi: 10.1001/jama.2013.282535
- 27. Neves PO, Andrade J, Monção H. Coronary artery calcium score: current status. *Radiol Bras.* (2017) 50(3):182–9. doi: 10.1590/0100-3984.2015.0235
- 28. Greenland P, Blaha MJ, Budoff MJ, Erbel R, Watson KE. Coronary calcium score and cardiovascular risk. *J Am Coll Cardiol.* (2018) 72(4):434–47. doi: 10.1016/j.jacc.2018.05.027
- 29. Villa-Bellosta R. Vascular calcification: key roles of phosphate and pyrophosphate. Int J Mol Sci. (2021) 22(24):13536. doi: 10.3390/ijms222413536
- 30. Wu Y, Ackerman JL, Strawich ES, Rey C, Kim HM, Glimcher MJ. Phosphate ions in bone: identification of a calcium-organic phosphate complex by 31p solid-state NMR spectroscopy at early stages of mineralization. *Calcif Tissue Int.* (2003) 72(5):610–26. doi: 10.1007/s00223-002-1068-8
- 31. Rey C, Collins B, Goehl T, Dickson IR, Glimcher MJ. The carbonate environment in bone mineral: a resolution-enhanced Fourier transform infrared spectroscopy study. *Calcif Tissue Int.* (1989) 45(3):157–64. doi: 10.1007/bf02556059
- 32. Rey C, Combes C, Drouet C, Glimcher MJ. Bone mineral: update on chemical composition and structure. *Osteoporos Int.* (2009) 20(6):1013–21. doi: 10.1007/s00198-009-0860-y
- 33. Orzechowska S, Wrobel A, Goncerz G, Podolec P, Rokita E. Physicochemical and micro-tomographic characterization of inorganic deposits associated with aortic stenosis. *J Heart Valve Dis.* (2014) 23:40–7.
- 34. Drouet C. Apatite formation: why it may not work as planned, and how to conclusively identify apatite compounds. *Biomed Res Int.* (2013) 2013:490946. doi: 10.1155/2013/490946
- 35. Larose E, Yeghiazarians Y, Libby P, Yucel EK, Aikawa M, Kacher DF, et al. Characterization of human atherosclerotic plaques by intravascular magnetic

resonance imaging. Circulation. (2005) 112(15):2324–31. doi: doi:10.1161/CIRCULATIONAHA.105.538942

- 36. Wang G, Zhang Y, Hegde SS, Bottomley PA. High-resolution and accelerated multi-parametric mapping with automated characterization of vessel disease using intravascular mri. *J Cardiovasc Magn Reson.* (2017) 19(1):89. doi: 10.1186/s12968-017-0399-6
- 37. Correia LCL, Atalar E, Kelemen MD, Ocali O, Hutchins GM, Fleg JL, et al. Intravascular magnetic resonance imaging of aortic atherosclerotic plaque composition. *Arterioscler, Thromb, Vasc Biol.* (1997) 17(12):3626–32. doi: doi:10.1161/01.ATV.17.12.3626
- 38. Larose E, Kinlay S, Selwyn AP, Yeghiazarians Y, Yucel EK, Kacher DF, et al. Improved characterization of atherosclerotic plaques by gadolinium contrast during intravascular magnetic resonance imaging of human arteries. *Atherosclerosis*. (2008) 196(2):919–25. doi: 10.1016/j.atherosclerosis.2007.02.020
- 39. O'Malley PG, Taylor AJ, Jackson JL, Doherty TM, Detrano RC. Prognostic value of coronary electron-beam computed tomography for coronary heart disease events in asymptomatic populations. *Am J Cardiol.* (2000) 85(8):945–8. doi: 10. 1016/s0002-9149(99)00906-6
- 40. van Soest G, Goderie TP, Gonzalo N, Koljenović S, van Leenders GL, Regar E, et al. Imaging atherosclerotic plaque composition with intracoronary optical coherence tomography. *Neth Heart J.* (2009) 17(11):448–50. doi: 10.1007/bf03086301
- 41. Hitchner E, Zayed MA, Lee G, Morrison D, Lane B, Zhou W. Intravascular ultrasound as a clinical adjunct for carotid plaque characterization. *J Vasc Surg.* (2014) 59(3):774–80. doi: 10.1016/j.jvs.2013.09.028
- 42. Ackerman JL. Chapter 15 solid state NMR spectroscopy. In: Macomber RS, editor. A Complete introduction to Modern NMR Spectroscopy. I. New York, NY: John Wiley & Sons Inc. (1997). p. 283–304.
- 43. Guo W, Morrisett JD, DeBakey ME, Lawrie GM, Hamilton JA. Quantification in situ of crystalline cholesterol and calcium phosphate hydroxyapatite in human atherosclerotic plaques by solid-state magic angle spinning nmr. Arterioscler, Thromb, Vasc Biol. (2000) 20(6):1630–6. doi: 10.1161/01.ATV.20.6.1630
- 44. Guo W, Morrisett JD, Lawrie GM, DeBakey ME, Hamilton JA. Identification of different lipid phases and calcium phosphate deposits in human carotid artery plaques by mas NMR spectroscopy. *Magn Reson Med.* (1998) 39(2):184–9. doi: 10.1002/mrm.1910390204
- 45. Ramanathan C, Ackerman JL. ADRF differential cross polarization spectroscopy of synthetic calcium phosphates and bone mineral. *J Magn Reson.* (1997) 127(1):26–35. doi: 10.1006/jmre.1997.1173
- 46. Ramanathan C, Wu Y, Pfleiderer B, Lizak MJ, Garrido L, Ackerman JL. Adrf-cp surface-coil spectroscopy of synthetic calcium phosphates and bone mineral. *J Magn Reson.* (1996) 121(2):127–38. doi: 10.1006/jmra.1996.0152
- 47. Wu Y, Glimcher MJ, Rey C, Ackerman JL. A unique protonated phosphate group in bone mineral not present in synthetic calcium phosphates. Identification by phosphorus-31 solid state NMR spectroscopy. *J Mol Biol.* (1994) 244(4):423–35. doi: 10.1006/jmbi.1994.1740
- 48. Wu Y, Chesler DA, Glimcher MJ, Garrido L, Wang J, Jiang HJ, et al. Multinuclear solid-state three-dimensional mri of bone and synthetic calcium phosphates. *Proc Natl Acad Sci U S A.* (1999) 96(4):1574–8. doi: 10.1073/pnas.96.4.1574
- 49. Weiger M, Stampanoni M, Pruessmann KP. Direct depiction of bone microstructure using mri with zero echo time. *Bone.* (2013) 54(1):44–7. doi: 10. 1016/j.bone.2013.01.027
- 50. Wu Y, Ackerman JL, Chesler DA, Graham L, Wang Y, Glimcher MJ. Density of organic matrix of native mineralized bone measured by water- and fat-suppressed proton projection MRI. *Magn Reson Med.* (2003) 50(1):59–68. doi: 10.1002/mrm.
- 51. Wu Y, Dai G, Ackerman JL, Hrovat MI, Glimcher MJ, Snyder BD, et al. Water-and fat-suppressed proton projection MRI (WASPI) of rat femur bone. *Magn Reson Med.* (2007) 57(3):554–67. doi: 10.1002/mrm.21174
- 52. Kuhn LT, Wu Y, Rey C, Gerstenfeld LC, Grynpas MD, Ackerman JL, et al. Structure, composition, and maturation of newly deposited calcium-phosphate crystals in chicken osteoblast cell cultures. *J Bone Miner Res.* (2000) 15(7):1301–9. doi: 10.1359/jbmr.2000.15.7.1301
- 53. Herzfeld J, Berger AE. Sideband intensities in NMR spectra of samples spinning at the magic angle. J Chem Phys. (1980) 73(12):6021–30. doi: 10.1063/1.440136
- 54. Yao J, Farrar CT, Aikawa E, Sosnovik DE, Moon BF, Kulkarni A, et al. *Ex vivo* phosphorus-31 solid-state magnetic resonance spectroscopy identifies compositional differences between bone mineral and calcified vascular tissues. *medRxiv* [Preprint]. *medRxiv:2025.09.27.25336805* (2025). Available online at: https://doi.org/10.1101/2025.09.27.25336805 (Accessed November 13, 2025).
- 55. van Meerten SGJ, Franssen WMJ, Kentgens APM. Ssnake: a cross-platform open-source NMR data processing and fitting application. *J Magn Reson.* (2019) 301:56–66. doi: 10.1016/j.jmr.2019.02.006
- 56. Arnold DL, Matthews PM, Radda GK. Metabolic recovery after exercise and the assessment of mitochondrial function *in vivo* in human skeletal muscle by means of <sup>31</sup>P NMR. *Magn Reson Med.* (1984) 1(3):307–15. doi: 10.1002/mrm. 1910010303

57. Moon RB, Richards JH. Determination of intracellular pH by <sup>31</sup>P magnetic resonance. *J Biol Chem.* (1973) 248(20):7276–8. doi: 10.1016/S0021-9258 (19)43389-9

- 58. Biltz RM, Pellegrino ED. The hydroxyl content of calcified tissue mineral. *Calcif Tissue Res.* (1971) 7(3):259–63. doi: 10.1007/bf02062614
- 59. Biltz RM, Pellegrino ED. The nature of bone carbonate. Clin Orthop Relat Res. (1977) 129:279–92. doi: 10.1097/00003086-197711000-00040
- 60. Wu Y, Ackerman JL, Kim HM, Rey C, Barroug A, Glimcher MJ. Nuclear magnetic resonance spin-spin relaxation of the crystals of bone, dental enamel, and synthetic hydroxyapatites. *J Bone Miner Res.* (2002) 17(3):472–80. doi: 10.1359/jbmr.2002.17.3.472
- 61. Aikawa E, Nahrendorf M, Figueiredo J-L, Swirski FK, Shtatland T, Kohler RH, et al. Osteogenesis associates with inflammation in early-stage atherosclerosis evaluated by molecular imaging *in vivo. Circulation.* (2007) 116(24):2841–50. doi: doi:10.1161/CIRCULATIONAHA.107.732867
- 62. Hutcheson JD, Goettsch C, Bertazzo S, Maldonado N, Ruiz JL, Goh W, et al. Genesis and growth of extracellular-vesicle-derived microcalcification in atherosclerotic plaques. *Nat Mater.* (2016) 15(3):335–43. doi: 10.1038/nmat4519
- 63. Xian JZ, Lu M, Fong F, Qiao R, Patel NR, Abeydeera D, et al. Statin effects on vascular calcification. *Arterioscler, Thromb, Vasc Biol.* (2021) 41(4):e185–e92. doi: 10. 1161/ATVBAHA.120.315737
- 64. Lei Y, Cui Q, Yang G, Piao L, Inoue A, Wu H, et al. Statins mitigate stress-related vascular aging and atherosclerosis in apoe-deficient mice fed high fat-diet: the role of glucagon-like peptide-1/adiponectin axis. *Front Cell Dev Biol.* (2021) 9:687868. doi: 10.3389/fcell.2021.687868
- 65. Nakamura K, Sasaki T, Cheng XW, Iguchi A, Sato K, Kuzuya M. Statin prevents plaque disruption in apoe-knockout mouse model through pleiotropic effect on acute inflammation. *Atherosclerosis*. (2009) 206(2):355–61. doi: 10.1016/j.atherosclerosis. 2009.02.014
- 66. Teo KK, Corsi DJ, Tam JW, Dumesnil JG, Chan KL. Lipid lowering on progression of mild to moderate aortic stenosis: meta-analysis of the randomized placebo-controlled clinical trials on 2344 patients. *Can J Cardiol.* (2011) 27(6):800-8. doi: 10.1016/j.cjca.2011.03.012
- 67. Baumgartner H, Falk V, Bax JJ, De Bonis M, Hamm C, Holm PJ, et al. 2017 ESC/EACTS guidelines for the management of valvular heart disease. *Eur Heart J.* (2017) 38(36):2739–91. doi: 10.1093/eurheartj/ehx391
- 68. Nishimura RA, Otto CM, Bonow RO, Carabello BA, Erwin JP 3rd, Guyton RA, et al. 2014 AHA/ACC guideline for the management of patients with valvular heart disease: executive summary: a report of the American College of Cardiology/ American Heart Association task force on practice guidelines. *Circulation*. (2014) 129(23):2440–92. doi: 10.1161/cir.0000000000000029
- 69. Arsenault BJ, Boekholdt SM, Mora S, DeMicco DA, Bao W, Tardif JC, et al. Impact of high-dose atorvastatin therapy and clinical risk factors on incident aortic valve stenosis in patients with cardiovascular disease (from TNT, IDEAL, and SPARCL). *Am J Cardiol*. (2014) 113(8):1378–82. doi: 10.1016/j.amjcard. 2014.01.414
- 70. Parolari A, Tremoli E, Cavallotti L, Trezzi M, Kassem S, Loardi C, et al. Do statins improve outcomes and delay the progression of non-rheumatic calcific aortic stenosis? *Heart.* (2011) 97(7):523–9. doi: 10.1136/hrt.2010.215046
- 71. Healy A, Berus JM, Christensen JL, Lee C, Mantsounga C, Dong W, et al. Statins disrupt macrophage rac1 regulation leading to increased atherosclerotic plaque calcification. *Arterioscler, Thromb, Vasc Biol.* (2020) 40(3):714–32. doi: 10.1161/ATVBAHA.119.313832
- 72. Tanaka K, Sata M, Fukuda D, Suematsu Y, Motomura N, Takamoto S, et al. Age-associated aortic stenosis in apolipoprotein e-deficient mice. *JACC*. (2005) 46(1):134–41. doi: 10.1016/j.jacc.2005.03.058
- 73. Farlay D, Panczer G, Rey C, Delmas PD, Boivin G. Mineral maturity and crystallinity index are distinct characteristics of bone mineral. *J Bone Miner Metab.* (2010) 28(4):433–45. doi: 10.1007/s00774-009-0146-7
- 74. Wang B, Zhang Z, Pan H. Bone apatite nanocrystal: crystalline structure, chemical composition, and architecture. *Biomimetics (Basel)*. (2023) 8(1):90. doi: 10.3390/biomimetics8010090
- 75. Iafisco M, Delgado López JM, Drouet C. Nanocrystalline apatites: synthesis, physical-chemical and thermodynamic characterization. In: Iafisco M, Delgado-Lopez JM, editors. *Apatites: Synthesis, Structural Characterization and Biomedical Applications*. New York: Nova Science Publishers (2014). Chapter 2, eBook, ISBN 978-1-63321-500-9
- 76. Von Euw S, Wang Y, Laurent G, Drouet C, Babonneau F, Nassif N, et al. Bone mineral: new insights into its chemical composition. *Sci Rep.* (2019) 9(1):8456. doi: 10.1038/s41598-019-44620-6
- 77. Bertolotti F, Carmona FJ, Dal Sasso G, Ramírez-Rodríguez GB, Delgado-López JM, Pedersen JS, et al. On the amorphous layer in bone mineral and biomimetic apatite: a combined small- and wide-angle x-ray scattering analysis. *Acta Biomater*. (2021) 120:167–80. doi: 10.1016/j.actbio.2020.04.026
- 78. Arnett T. Extracellular ph regulates bone cell function. J Nutr. (2008) 138:415S–8. doi: 10.1093/jn/138.2.415S

- 79. Liu CL, Zhang X, Liu J, Wang Y, Sukhova GK, Wojtkiewicz GR, et al. Na(+)-h (+) exchanger 1 determines atherosclerotic lesion acidification and promotes atherogenesis. *Nat Commun.* (2019) 10(1):3978. doi: 10.1038/s41467-019-11983-3
- 80. Ma J, Zhao X, Xu X, Lixin A, Liu Q, Qu P. A bibliometric analysis of strategies for atherosclerosis treatment with organic nanoparticles. *Pharmaceutics*. (2025) 17(9):1131. doi: 10.3390/pharmaceutics17091131
- 81. Naghavi M, John R, Naguib S, Siadaty M, Grasu R, Kurian K, et al. pH heterogeneity of human and rabbit atherosclerotic plaques; a new insight into detection of vulnerable plaque. Atherosclerosis. (2002) 164:27–35. doi: 10.1016/S0021-9150(02)00018-7
- 82. Campbell-Washburn AE, Varghese J, Nayak KS, Ramasawmy R, Simonetti OP. Cardiac mri at low field strengths. *J Magn Reson Imaging*. (2024) 59(2):412–30. doi: 10.1002/jmri.28890
- 83. Campbell-Washburn AE, Ramasawmy R, Restivo MC, Bhattacharya I, Basar B, Herzka DA, et al. Opportunities in interventional and diagnostic imaging by using high-performance low-field-strength MRI. *Radiology.* (2019) 293(2):384–93. doi: 10. 1148/radiol.2019190452
- 84. Nardi-Schreiber A, Gamliel A, Harris T, Sapir G, Sosna J, Gomori JM, et al. Biochemical phosphates observed using hyperpolarized 31p in physiological aqueous solutions. *Nat Commun.* (2017) 8(1):341. doi: 10.1038/s41467-017-00364-3
- 85. Espitia O, Chatelais M, Steenman M, Charrier C, Maurel B, Georges S, et al. Implication of molecular vascular smooth muscle cell heterogeneity among arterial beds in arterial calcification. *PLoS One.* (2018) 13(1):e0191976. doi: 10.1371/journal.pone.0191976